The Astrophysical Journal, 946:64 (9pp), 2023 April 1 https://doi.org/10.3847/1538-4357/acbc15

The Initiation and Back-reaction of the X5.4 Flare on 2012 March 7

Nian Liu[1], Ju Jing[1,2], Qiang Hu[3], Satoshi Inoue[1], and Haimin Wang[1,2]
[1] Institute for Space Weather Sciences, New Jersey Institute of Technology, Newark, NJ 07102-1982, USA; nl244@njit.edu
[2] Big Bear Solar Observatory, New Jersey Institute of Technology, 40386 North Shore Lane, Big Bear City, CA 92314-9672, USA
[3] Department of Space Science and CSPAR, The University of Alabama in Huntsville, Huntsville, AL 35899, USA
Received 2022 July 24; revised 2023 February 13; accepted 2023 February 13; published 2023 March 30

Abstract

In this paper, we study the evolution of the X5.4 flare (SOL2012-03-07T00:02) in NOAA Active Region 11429, focusing on its initiation mechanisms and back-reaction effects. To help our study, three-dimensional (3D) coronal magnetic field models are extrapolated from the photospheric magnetograms of the Helioseismic and Magnetic Imager on board the Solar Dynamics Observatory under the assumptions of nonlinear force-free field (NLFFF) and non-force-free field (non-FFF). We investigate the 3D magnetic structure and MHD kink instability, torus instability, and double-arc instability (DAI), and find that this flare is most likely triggered by the tether-cutting reconnection and the subsequent DAI. For the back-reactions of the flare, both NLFFF and non-FFF models clearly show an increase in horizontal magnetic field (B_h) and a decrease in inclination angle (ϕ) of the magnetic field near the polarity inversion line, from the photosphere up to a certain height (5 Mm and 8 Mm for non-FFF and NLFFF, respectively). In addition, the non-FFF model shows an enhancement of the downward Lorentz force acting on the photosphere, and the location of the enhancement spatially coincides with the location of the flare onset. The observed back-reaction is likely a consequence of magnetic reconnection.

Unified Astronomy Thesaurus concepts: Solar flares (1496); Solar activity (1475); Solar active region magnetic fields (1975)

1. Introduction

The triggering and driving mechanisms of solar eruptions have been an important question in the study of space weather, which is strongly related to modern human activities. However, it has not been well answered. Generally speaking, the two processes, magnetohydrodynamic (MHD) instability and magnetic reconnection, may work simultaneously in triggering and driving an eruption. Mechanisms commonly thought to trigger solar eruptions and produce coronal mass ejections (CMEs) include tether-cutting reconnection (Moore et al. 2001), magnetic breakout reconnection (Antiochos et al. 1999; MacNeice et al. 2004), MHD helical kink instability (KI, Bateman 1978; Török et al. 2004), MHD torus instability (TI, Kliem & Török 2006), sunspot rotation (Amari et al. 1996; Tokman & Bellan 2002), etc.

Specifically, TI occurs when the strapping magnetic field above a magnetic flux rope (MFR) structure decays with height at a sufficiently fast rate, as quantified by the decay index:

$$n \equiv -\frac{\partial \log(\boldsymbol{B}_{\rm ext})}{\partial \log(h)}, \tag{1}$$

where $\boldsymbol{B}_{\rm ext}$ denotes the external strapping field, usually assumed to be the horizontal component of the potential field. Numerical analysis shows that the critical threshold of n is $n_{\rm crit} = 1.5$ (Bateman 1978; Kliem & Török 2006), beyond which the MFR is unstable due to TI.

The KI, on the other hand, is expected to lead to the deformation of an MFR when the winding number of magnetic field lines around the MFR axis exceeds a critical value $T_{w,\rm crit}$. The twist of an MFR can be calculated by using the twist number T_w as a proxy:

$$T_w = \int_L \frac{\mu_0 J_{||}}{4\pi |B|} dl, \tag{2}$$

where $J_{||}$ is the parallel component of current density in the direction of the magnetic field.

The tether-cutting reconnection proposed by Moore et al. (2001) is a widely accepted model for solar eruptions. Its scenario is characterized by a "sigmoid-to-arcade" and a "four footpoints to two ribbons" evolution (Liu et al. 2007, 2013). That is, the reconnection of two sheared arcades leads to the formation of a low-lying shorter loop across the magnetic polarity inversion line (PIL) and a longer MFR connecting the two distant ends of a sigmoid. The tether-cutting reconnection below the newly formed MFR gradually transforms the shear arcade into the MFR, which eventually becomes unstable due to the attenuated stabilizing effect of the overlying magnetic field.

Recently, a double-arc instability (DAI) has been proposed by Ishiguro & Kusano (2017), which has the same topology as the tether-cutting reconnection, but the long magnetic loop formed by the tether-cutting reconnection has a double-arc shape. Such a double-arc loop implies an additional upward Lorentz force and is therefore more susceptible to instability. DAI occurs when a magnetic parameter κ exceeds a threshold of the order of $\kappa_0 = 0.1$, derived from MHD numerical analysis (Ishiguro & Kusano 2017). κ is defined as

$$\kappa \equiv T_w \frac{\Phi_{\rm rec}}{\Phi_{\rm tot}}, \tag{3}$$

where $\Phi_{\rm rec}$ and $\Phi_{\rm tot}$ are the magnetic flux of the double-arc loops and the total flux of the external strapping field, respectively. Furthermore, the minimum area with $\kappa \geqslant \kappa_0$ can

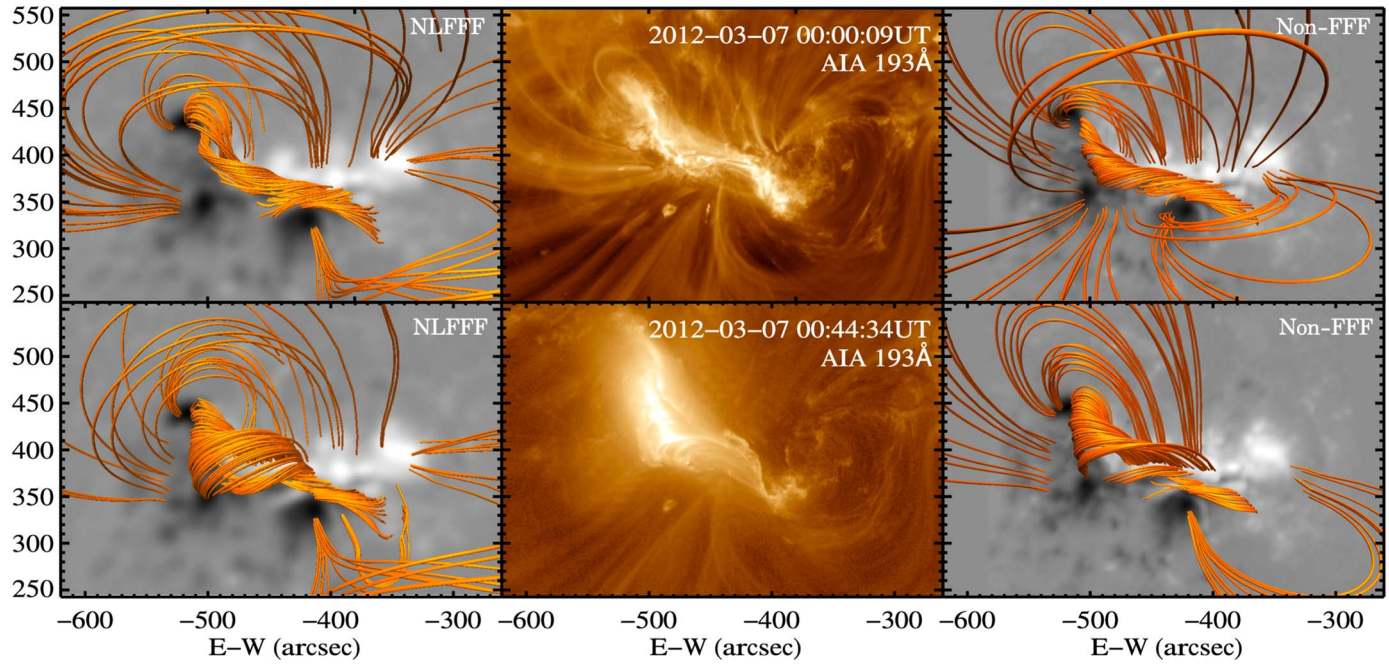

Figure 1. 3D visualized magnetic field lines of NLFFF and non-FFF. The upper panels and lower panels show the extrapolation results one hour before and one hour after the flare, respectively. The middle panels show the AIA/EUV 193 Å channel images 2 minutes before and 40 minutes after the flare start time.

also help us pinpoint the location of the flare onset (Kusano et al. 2020).

On the other hand, the concept of back-reaction due to energy release from the coronal fields was introduced by Hudson et al. (2008) and Fisher et al. (2012). Based on the simple principle that the abrupt force perturbations during eruptions should be balanced by equal and opposite force perturbations acting on the solar photosphere and interior, Fisher et al. (2012) introduced a practical formulation to calculate the change in Lorentz force acting on the solar photosphere through photospheric magnetic measurements. The change in downward Lorentz force acting on the photospheric layer and the solar interior after the flare is also predicted so that the photospheric magnetic field becomes more horizontal. Many observations confirm such a change (Spirock et al. 2002; Wang et al. 2002, 2004, 2012a, 2012b, 2014; Wang 2006; Wang & Liu 2010; Gosain 2012; Petrie 2012, 2019; Sun et al. 2012).

In this paper, we investigate the initiation and back-reaction of the X5.4 flare (SOL205-03-07T00:02) in NOAA Active Region 11429. The nonlinear force-free field (NLFFF, Wheatland et al. 2000; Wiegelmann 2004) model and the newly developed non-force-free field (non-FFF, Hu & Dasgupta 2008; Prasad et al. 2017) model are used to help us understand the 3D coronal magnetic field. The observations and modeling details are given in Section 2, and our results and discussion are given in Section 3 and Section 4, respectively.

2. Observation and Modeling

The X5.4 flare started at 00:02 UT on 2012 March 7, in NOAA AR 11429, and its soft X-ray emission peaked at 00:24 UT. The extreme ultraviolet (EUV) observation obtained from the Atmospheric Imaging Assembly on board the Solar Dynamics Observatory (SDO/AIA, Lemen et al. 2012) shows that the major topology of the AR is a sigmoidal configuration before the flare (see middle panels in Figure 1). The EUV emissions of the flare initially appeared as precursor brightenings along both sides of the PIL. Then the brightening areas were connected and formed two clear ribbons and expanded away from the PIL. A clear arcade connecting two ribbons was observed about 10 minutes after the flare start time.

Considering different purposes of the analysis, two coronal magnetic field models, the NLFFF and non-FFF models, were extrapolated. The former is a viable model for reconstructing the coronal magnetic field of solar ARs and has been extensively applied in many previous studies on the instability of ARs. The latter has the advantage that it can be used to gauge the variation of the Lorentz force in the back-reaction process, but it is not yet as well validated as the former. Therefore, here we mainly use the NLFFF model to study the magnetic field configuration associated with flare initiation and back-reaction, while the non-FFF model is only used to study the variation of the Lorentz force during the back-reaction process.

The NLFFF extrapolation was performed with the weighted optimization method, which minimizes a volume integral of both Lorentz force and field divergence (Wiegelmann 2004). Prior to the NLFFF extrapolation, a preprocessing scheme (Wiegelmann et al. 2006) was applied to the lower boundary data to make the photospheric boundary more compatible with the force-free assumption. Due to the force-free nature of the NLFFF model, it cannot be used to examine the variation of Lorentz force in the back-reaction studies, and this gap can be filled by the non-FFF model.

The non-FFF extrapolation technique numerically decomposes the coronal magnetic field into three vector components (Hu & Dasgupta 2006, 2008): one potential (current-free) component and two distinct linear force-free field (LFFF) components, $B = \boldsymbol{B}_1 + \boldsymbol{B}_2 + \boldsymbol{B}_{\rm pot}$, with $\nabla \times \boldsymbol{B}_i = \alpha_i \boldsymbol{B}_i$, $i = 1, 2$, and $\alpha_1 \neq \alpha_2 \neq 0$. In this case, the summation of these three components is not force-free ($\nabla \times \boldsymbol{B} \times \boldsymbol{B} \neq 0$), even though each component itself is force-free. This approach requires two

layers of vector magnetic field on the solar surface as inputs. Hu et al. (2008) improved this method by adding a coefficient constant in the potential field term as $c\boldsymbol{B}_{\rm pot}$ where $c \in [-1, 1]$ with $\boldsymbol{B}_{\rm pot}$ known so that only one layer of input is required. However, it still has a limitation on real magnetograph measurements for $c\boldsymbol{B}_{\rm pot}$ is only a special potential field proportional to the potential field obtained from the input photospheric magnetogram. Therefore, Hu et al. (2010) further improved the algorithm by substituting a corrector subfield $\boldsymbol{B}_{\rm pot} = \sum \boldsymbol{B}^{(k)}_{\rm pot}$, $k = 1, 2, 3, ...$, through an iterative approach, taking advantage of the fact that the summation of a series of potential fields remains potential. With this approach, only a one-layer photospheric vector magnetogram is used as input without preprocessing.

According to Hu et al. (2010), the non-FFF results indicate that the nonvanishing Lorentz force mainly exists in the low corona. In an example in Hu et al. (2010), the Lorentz force decreased to 10% of its photospheric value at the height of ~2 Mm. The NLFFF extrapolation, on the other hand, is only applicable to regions of low plasma β where the force-free assumption is justified. As mentioned, we used a step called preprocessing (Wiegelmann et al. 2006) to remove the net force and torque while smoothing the observed photospheric magnetic field. In this way, the NLFFF model can also reproduce magnetic fields well in the near-surface region at the expense of spatial resolution.

We use the photospheric vector magnetogram *hmi.B_135s_series* data, obtained from the Helioseismic and Magnetic Imager (HMI, Scherrer et al. 2012) on board the SDO (Pesnell et al. 2012), as the boundary condition to extrapolate a time sequence of NLFFFs and non-FFFs at a cadence of 135 s. Depending on the purpose of the analysis, we chose to use different spatial resolutions and fields of view (FOVs) for the extrapolation. An FOV of $400'' \times 400''$ with a pixel scale of $1''$ was applied in the NLFFF and non-FFF extrapolations to obtain the overall magnetic field topology of the AR for comparison with the EUV observations. As an example, Figure 1 shows the coronal magnetic fields extrapolated from both NLFFF (left column) and non-FFF (right column) models before and after the flare, in comparison with the AIA/EUV 193 Å observation (middle column). The AIA observations show the sigmoid-to-arcade evolution, which is consistent with the tether-cutting reconnection scenario. Both models generally agree well with the AIA 193 Å observations. A smaller FOV of $200'' \times 200''$ with a pixel scale of $0.5''$ was chosen for the NLFFF extrapolation to demonstrate the fine magnetic field structure in the initiation phase as shown in Figure 3. The small FOV ($200'' \times 200''$) and $1''$ per pixel grid resolution are applied to the NLFFF and non-FFF to obtain the changes in magnetic field in the back-reaction phase as shown in Figures 4–6.

3. Results

Our focus is on the initiation and the back-reaction of the flare, both of which are given in the following subsections.

3.1. Initiation

To identify the possible trigger mechanisms of the flare, we study the preflare magnetic field conditions. The preflare NLFFF model clearly exhibits the presence of a current-carrying MFR prior to the flare, as shown in Figure 2. The MFR is oriented along the PIL and is cospatial with the bright emission in the AIA 304 Å image. The critical threshold of decay index $n_{\rm crit}$ for TI is 1.5 (Bateman 1978; Kliem & Török 2006). In this case, however, only n at the top of the MFR can reach 1.1, and the vast majority of the MFR is in the region where the n value is below 1. This suggests that the external strapping magnetic field has a strong constraining effect on the MFR and that TI is unlikely to be the main triggering/driving mechanism for this eruption.

On the other hand, this MFR is moderately to highly twisted, with $|T_w|$ values mostly in the range 0.5–1. Some magnetic field lines have $|T_w|$ values even up to 2 (see Figure 3), which exceeds the critical value ($T_{w,\rm crit} = 1.25$) of KI in numerical models (Baty 2001; Török & Kliem 2003). However, $T_{w,\rm crit} = 1.25$ is the minimum requirement in MHD simulations with a twist value uniformly distributed along a straight MFR. In this study, the twist number is not uniform, and not greater than 1.25 along most parts of the MFRs produced by NLFFF. Furthermore, the geometry of an MFR, rather than being in a simple line-tied shape, is more complicated in that two footpoints are anchored on the solar surface, which requires a larger twist to cause the KI. Therefore, the KI is not guaranteed to occur, and we did not find any indication in AIA/EUV observations corresponding to the occurrence of KI. Instead, we found signs of tether-cutting reconnection.

We mentioned earlier that the transition of the coronal magnetic field from sigmoid to arcade, as shown in Figure 1, is consistent with the tether-cutting reconnection scenario. In addition, as shown in Figure 3(a), four small flare precursors (denoted by p1, p2, n1, n2) are distributed on both sides of the PIL, which is also an important observational feature of the tether-cutting reconnection. The magnetic lines coming out of precursors are divided into four groups, according to the position of their footpoints, p1n1, p2n1, p1n2, and p2n2, respectively. Figures 3(b) and (c) show the variation of the four groups of the MFR before and after the flare starts. It appears that the loops of p1n1 and p2n2 increase, suggesting that some of the magnetic field lines of n1p2 and n2p1 are reconnected to form p1n1 and p2n2.

DAI is one of possible trigger mechanisms recently proposed by Ishiguro & Kusano (2017). The topology of the DAI scenario is the same as that of the tether-cutting reconnection. It shows that when the κ parameter exceeds a threshold value of 0.1, the double-arc loop structure due to the tether-cutting reconnection becomes unstable in the joint region bridging the two systems of reconnected sheared loops. A previous study by Kusano et al. (2020) used the κ-scheme method to predict the initiation location of this flare, which is on one of the precursors and marked by the small circle in Figure 3(a). Here we investigate the possibility of DAI triggering this flare by estimating κ in Equation (3). Since it is difficult to derive $\Phi_{\rm rec}$ through observations, we follow the approach in Muhamad et al. (2018) and assume that the double-arc loop is formed by reconnection between twisted lines with T_w exceeding the critical threshold (T_c):

$$\kappa_{T_c} = \frac{\int_{T_w/T_c>1} |T_w|\, d\Phi}{\Phi_{\rm tot}}, \tag{4}$$

where $d\Phi = |B_r| dS$ and T_c is the threshold twist number value of the applied field lines in the formula. To estimate $\Phi_{\rm tot}$, we first select the magnetic field at $|B_z| > 300$ G (indicated by the contour in Figure 2(e)) and extrapolate the field lines from the

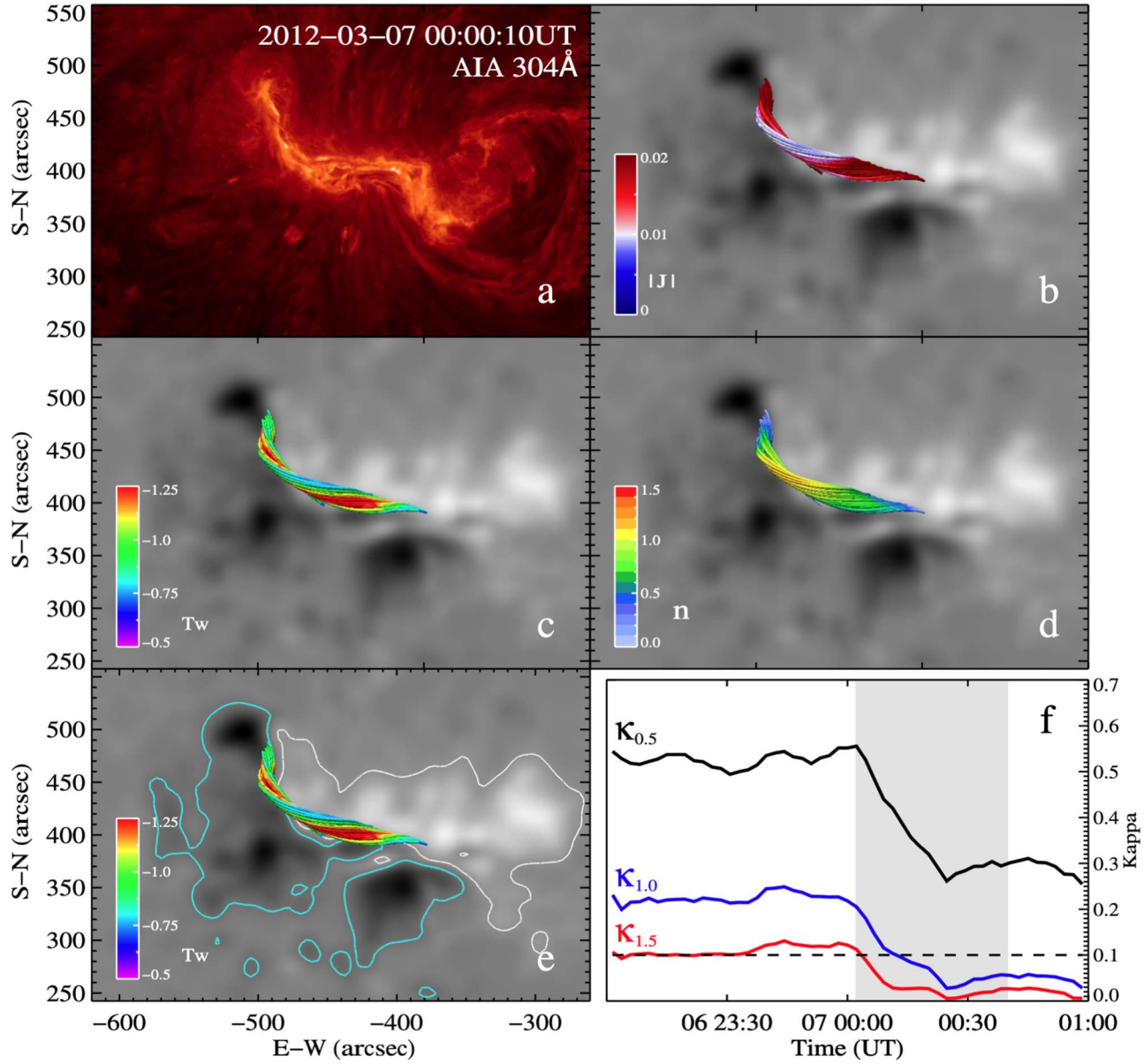

Figure 2. NLFFF results of the internal magnetic field at one hour before the flare. (a) Chromospheric AIA/EUV observation at 304 Å at 2 minutes before the flare. (b)–(d) Internal field lines with different colors showing the intensity of current density (A m^{-2}), twist number, and decay index, respectively. (e) MFR of high twist values; the white and cyan contours indicate the areas selected in the calculation of κ where the vertical magnetic field intensity is greater than 300 G. (f) Time variations of κ values with different threshold twist numbers (T_c). The shaded area in panel (f) indicates the flare period.

negative-polarity field closer to the MFR. We then include in the calculation the extrapolated field lines that satisfy the following conditions: (1) the other end of the field line lies within the selected field of positive polarity shown by the white contour in Figure 2(e), (2) the top of the field line exceeds the top of the MFR (∼10 Mm), and (3) the connecting segment at each end of the field line spans the MFR. This approach is similar to that used by Muhamad et al. (2017), but with more conditions for selecting the field lines.

The three κ_{Tc} time variations, corresponding to three values of T_c of 0.5, 1.0, and 1.5, respectively, are presented in Figure 2(f). All three profiles declined significantly after the flare onset. $\kappa_{1.0}$ and $\kappa_{1.5}$, but not $\kappa_{0.5}$, both drop below the DAI threshold $\kappa_{\rm crit} \simeq 0.1$. This suggests that DAI may be responsible for triggering the flare.

3.2. Back-reaction

As the result of the coronal field restructuring that is required to release magnetic energy and the conservation of momentum, the back-reactions are expected as the photospheric magnetic fields become more horizontal after flares (Hudson et al. 2008). Previous observational evidence for back-reactions is abundant, such as the enhancement of the photospheric horizontal magnetic field after the flare onset (Wang & Liu 2010; Wang et al. 2012b, 2014). Here, we investigate the evolution of horizontal magnetic fields with a time series of NLFFF models. Figure 4 shows the enhancement of the horizontal magnetic field after this flare, with the most significant changes occurring around the PIL. As shown in Figure 4(a), the B_h profiles start to rise within 5 minutes after the flare start time. Even after soft X-ray emission from the flare reached its peak, indicated by the

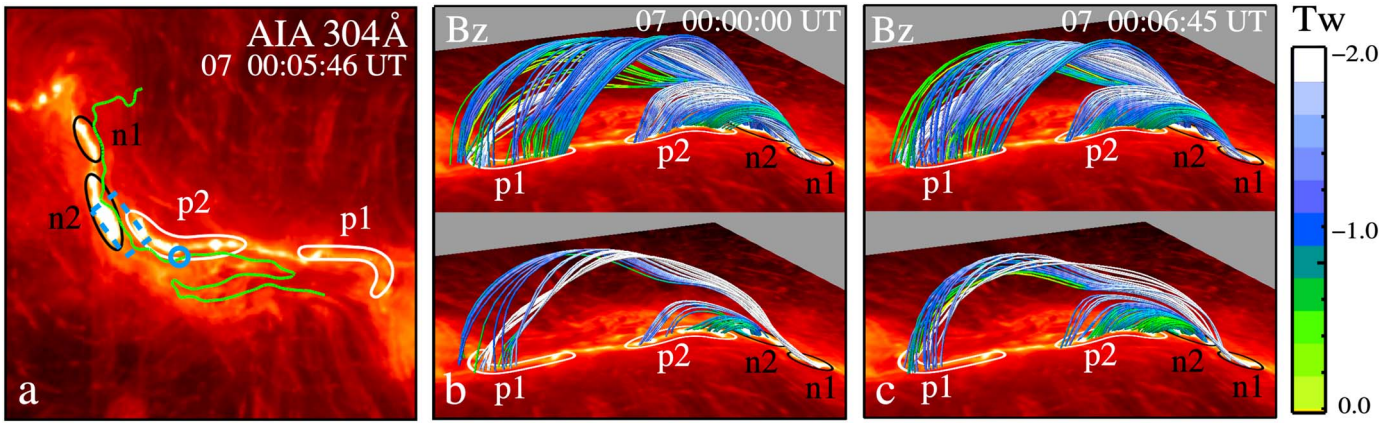

Figure 3. The high-resolution NLFFF MFRs overplotted on the AIA/EUV 304 Å images. The green curve in panel (a) indicates the PILs. The white and black contours denoted as p1, p2, n1, and n2 in all panels show the four footpoints of MFRs of positive and negative polarity, respectively. The blue box and circle in panel (a) mark the position of the region of interest (ROI) in the back-reaction study in Section 3.2 and the initiation location determined in Kusano et al. (2020), respectively. The top panels of (b) and (c) show the MFRs of both p1n2 and p2n1 before and after the reconnection. Similarly, the bottom panels of (b) and (c) show the MFRs of both p1n1 and p2n2. All the MFRs in (b) and (c) are colored with the intensity of the twist number values.

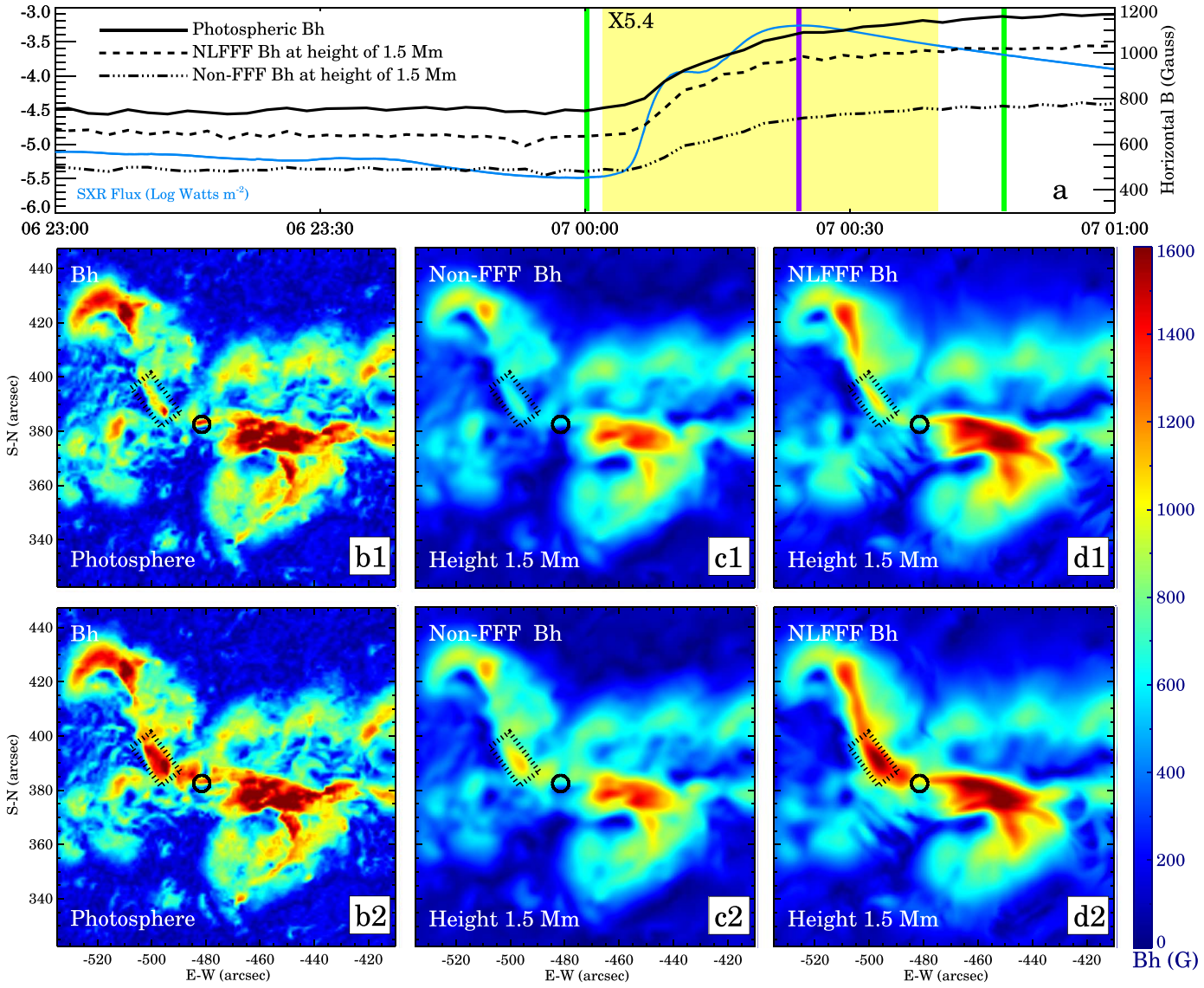

Figure 4. Variations in horizontal magnetic field in the photosphere and at the height of 1.5 Mm of NLFFF and non-FFF results, before and after the flare. (a) Time profiles of GOES soft X-rays (SXR) and the variations of averaged B_h within the ROI. The yellow shaded area indicates the flare period. Two green vertical lines show the times of panels (b1)–(d1) and panels (b2)–(d2), respectively. The purple line indicates the flare peak time. The black boxes and circles in panels (b1)–(d2) mark the position of the ROI in this study and the initiation location determined in Kusano et al. (2020), respectively.

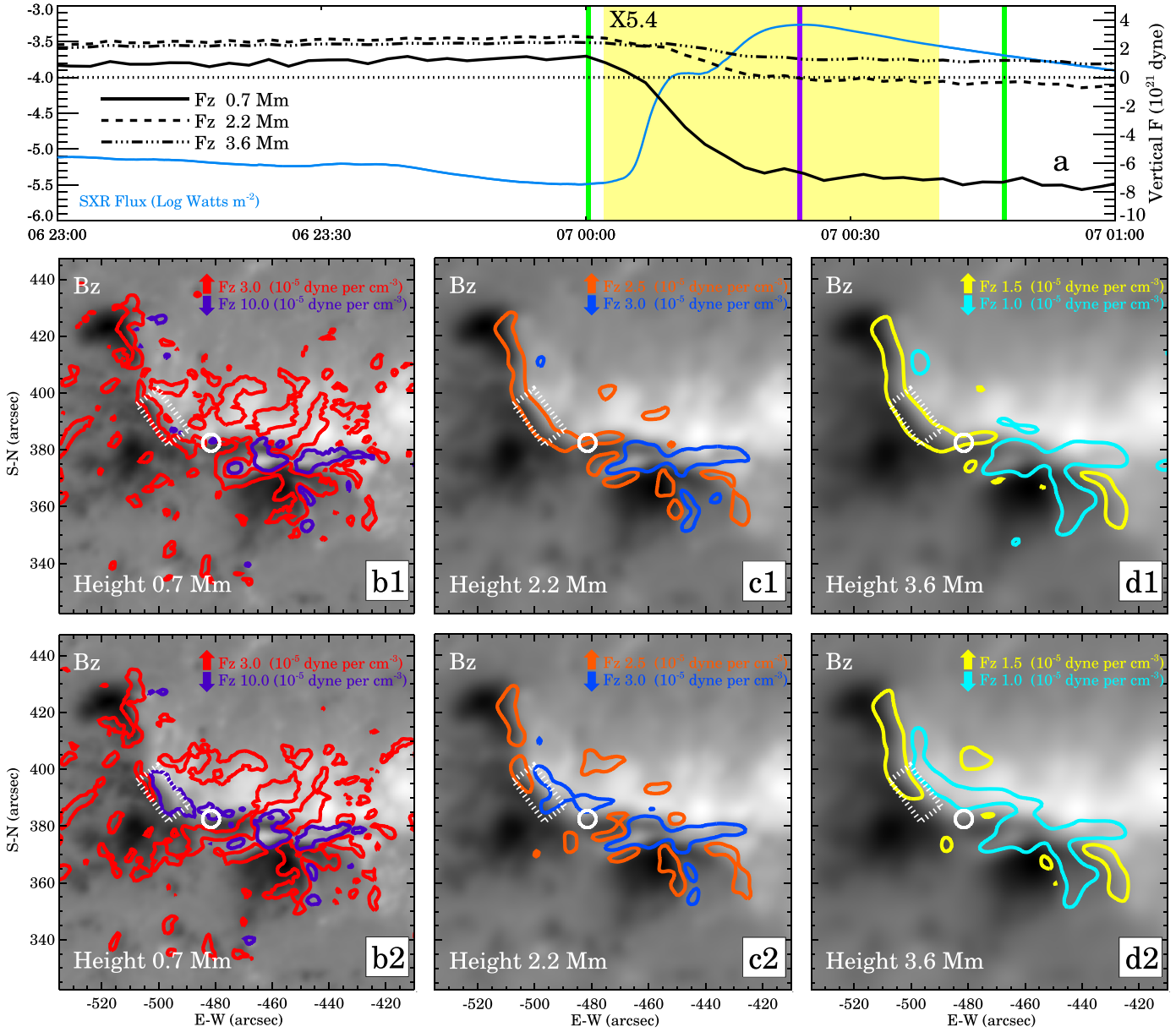

Figure 5. Variations in vertical Lorentz force at the heights of 0.7 Mm, 2.2 Mm, and 3.6 Mm of non-FFF results, before and after the flare. (a) Time profiles of GOES SXR and F_z variations within the ROI. The yellow shaded area indicates the flare period. Two green vertical lines show the times of panels (b1)–(d1) and panels (b2)–(d2), respectively. The purple line indicates the flare peak time. The white boxes and circles in panels (b1)–(d2) mark the position of the ROI in this study and the initiation location determined in Kusano et al. (2020), respectively. The different colors of the contours in panels (b1)–(d2) indicated the different directions and magnitudes of F_z.

purple line, the B_h time profiles still show an enhancement at a slower rate until one hour after the flare. The enhancement in B_h is not only seen in the photospheric layer, but also in a certain height range above the photosphere. As an example, the variations of the horizontal magnetic field in the non-FFF and NLFFF models at a height of 1.5 Mm above the photosphere are shown in Figures 4(c1) and (c2) and Figures 4(d1) and (d2), respectively. A similar B_h enhancement is evident in both the NLFFF and non-FFF models, but the latter shows weaker changes.

The non-FFF model allows us to calculate the Lorentz force, i.e.,

$$\boldsymbol{F} = -\frac{1}{4\pi}\int_V \nabla \times \boldsymbol{B} \times \boldsymbol{B}\, dV. \quad (5)$$

Figure 5(a) shows the temporal evolution of the vertical Lorentz force (F_z) at three selected altitudes, averaged over a small ROI marked by the rectangle in the middle and bottom panels. This ROI is along the PIL and mainly at the location of precursors p2 and n2. The average value of F_z at all three altitudes shows a significant decrease after the onset of the flare, suggesting the enhancement of downward Lorentz force. The higher the altitude, the smaller the magnitude of the change and the later the change appears. In the middle and bottom panels, we can see a decrease in the area of the upward F_z and an increase in the area of the downward F_z in the ROI.

Figure 6 further shows the variations of averaged F_z, B_h, and inclination angle ϕ (the angle between the magnetic field and the horizontal direction) within the ROI with time and altitude. The consequences of back-reaction are clearly shown in both

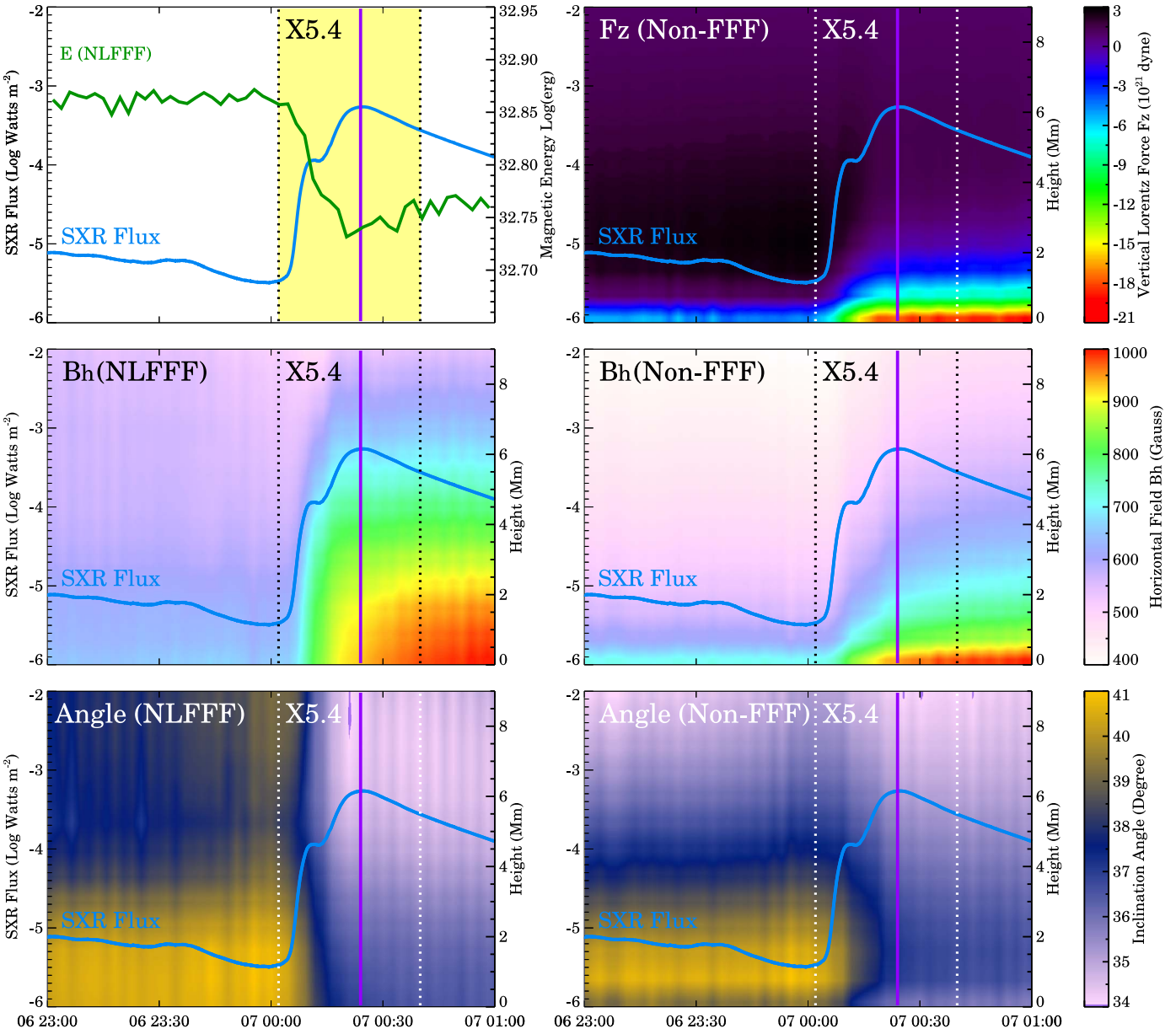

Figure 6. The time variations of F_z from non-FFF, B_h, and ϕ from both NLFFF and non-FFF within the height limit of 10 Mm of the ROI. The upper left panel shows the time profiles of GOES SXR and the magnetic free energy of NLFFF. The yellow shaded area indicates the flare period. The vertical dashed lines and purple lines in each panel mark the flare start time, end time, and peak time, respectively.

NLFFF and non-FFF models, i.e., an increase in B_h and a decrease in ϕ. In addition, non-FFF shows an obvious increasing downward F_z in the near-surface region.

However, there are non-negligible differences between the two models in the range of altitudes affected by the back-reaction. The NLFFF exhibits distinguishable back-reaction at ~8 Mm and below, while in the non-FFF model, the back-reaction is affected in the range below 5 Mm. More discussion about the differences between NLFFF and non-FFF is presented in Section 4.

4. Conclusion and Discussion

In summary, we investigated the initiation and back-reaction of the X5.4 flare on 2012 March 7, and our main results are as follows.

1. The X5.4 flare eruption is triggered by the tether-cutting reconnection and the subsequent DAI. The MFRs are continuously raised due to DAI until the TI takes over at the altitude where the decay index is sufficiently large to eventually drive the eruption.
2. The back-reaction effects, manifested as enhancement of horizontal field and decrease of inclination angle, are observed over a certain altitude range, which is 0–8 Mm for the NLFFF model and 0–5 Mm for the non-FFF model. In addition, the non-FFF model shows an increased downward Lorentz force at low altitudes, 0–2 Mm.

We find strongly twisted field lines ($|T_w| \sim 2$) as early as 2 hr before the flare, which could possibly cause KI. However, there is no observational evidence from the AIA/EUV to support the occurrence of KI. The slowly decaying strapping fields likely

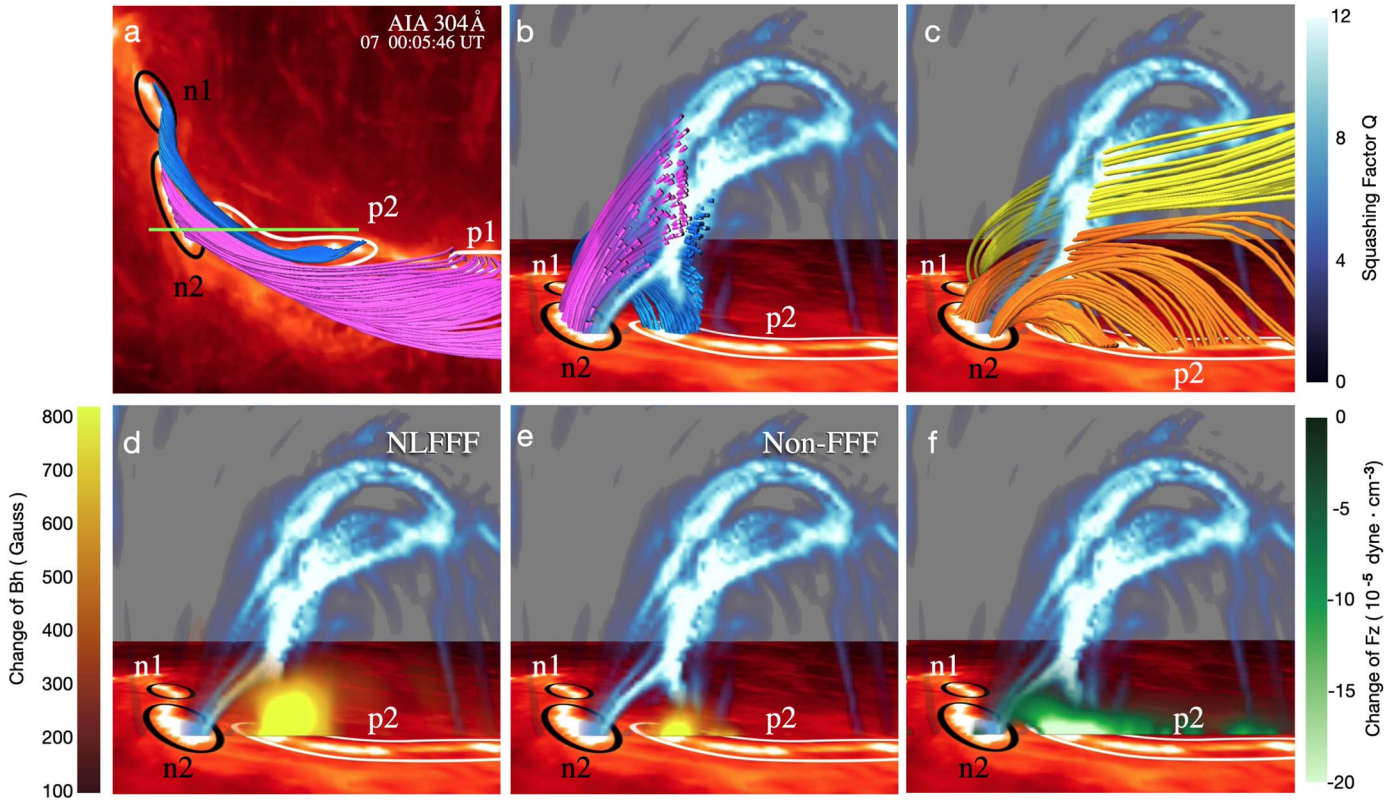

Figure 7. The changes in the magnetic field before and after the flare (at 00:00 UT and 00:58 UT on March 7, respectively). (a) An AIA 304 Å image superimposed with four footpoint contours p1, n1, p2, and n2 (same as in Figure 3(a)) and NLFF field lines. The green line indicates the position of the vertical cross section shown in panels (b)–(f). (b) The vertical distribution of the squashing factor (Q) derived from the NLFFF model. The field lines are colored purple and blue, representing p1n2 and p2n1 connectivity, respectively, at 00:00 UT on 2012 March 7. (c) Same as (b), but the field lines colored yellow and orange are p1n1 and p2n2 connectivity, respectively, at 00:06 UT on 2012 March 7. (d), (e) Same as (b) without the NLFF field lines, but including the change in the horizontal magnetic field (dB_h) derived from the NLFFF and non-FFF models, respectively. (f) Same as (b) without the NLFF field lines, but including the change in Lorentz force (dF_z).

play a role in preventing the eruption due to KI. Instead, we find the evolution of "four footpoints to two ribbons," which is a key feature of the tether-cutting reconnection. In the NLFFF, the 3D magnetic configuration is also consistent with the magnetic configuration in the tether-cutting reconnection. The long loops connecting the two far ends of the sigmoid appear to be a double-arc MFR with enhanced strong current density, as in DAI. It is evident that the double MFR is in the torus-stable region, but its κ parameter characterizing DAI exceeds the critical threshold for DAI before the flare and then drops below the threshold after the flare starts. These features indicate that the tether-cutting reconnection and the subsequent DAI would be responsible for initiating the flare. In this study, we identify the initiation location to be where tether-cutting reconnection happens, which should cover the PIL between n2 and p2 in Figure 3(a). On the other hand, Kusano et al. (2020) predicted the location of the flare onset using the κ scheme in DAI shown by the circles in Figures 3–5, which overlapped with the p2 region in this study. In general, these two studies show consistent results in terms of finding the location of tether-cutting reconnection.

The Lorentz force in the corona has rarely been studied before, as the coronal magnetic field is not available from observations, and the NLFFF model, which is usually used to study the coronal magnetic field, is inherently not applicable to the calculation of the Lorentz force. In this study, we use the non-FFF model to derive the 3D spatial distribution of the Lorentz force and find an increase in the downward Lorentz force, which, together with the enhanced horizontal magnetic field and decreased inclination angle, confirms the concept of back-reaction of coronal restructuring. To the best of our knowledge, this is the first application of the non-FFF model to the analysis of the Lorentz force in the 3D solar magnetic field. In addition to the unique advantage of calculating Lorentz forces, the non-FFF model also reproduces reasonably well the magnetic field in the near-surface region.

It is worth noting that the location of the flare initiation is also the location where the back-reaction is particularly significant. As shown in Figures 3–5, the most significant back-reaction occurs in the dashed box, which overlaps part of p2 and n2 and the PIL in between. In the tether-cutting reconnection scenario, the magnetic field becomes more horizontal near the PIL and the surface, due to the newly formed short loops there. In that same area, the vertical Lorentz force changes accordingly. This result is in agreement with the expectations of the back-reaction theory and has been demonstrated with the evolution of 3D magnetic fields in this study.

The increase in B_h and decrease in F_z may be caused by a change in downward momentum and/or by a topological change due to magnetic reconnection. In an attempt to understand the role of magnetic reconnection in the back-reaction mechanism, Figure 7 shows the changes in magnetic field connectivity in a vertical cross section shown by the squash factor (Q), together with the changes in vertical Lorentz force (dF_z) and the horizontal magnetic field (dB_h) before and after the flare. In the quasi-separatrix theory proposed by

Priest & Demoulin (1995), the magnetic reconnection preferably occurs on quasi-separatrix layers (QSLs), which could be identified by the high squashing factor Q (Titov et al. 2002). Figure 7(b) shows that the two MFRs of p1n2 and p2n1 are clearly separated by a QSL with $Q > 12$, indicating that magnetic reconnection between p1n2 and p2n1 is highly expected. Figure 3(c) further confirms such expectation by showing the enhanced MFRs (p1n1 and p2n2) as the result of the tether-cutting reconnection passing through the areas of strongest Q. The distribution of Q also shows an arched structure connecting the two footpoints p2 and n2 (Figure 7(b)), which is consistent with our observation of an MFR p2n2 enhanced by magnetic field reconnection after the flare (see Figure 3). The strongest back-reaction, shown as the strongest dB_h and dF_z, is spatially concentrated at the footpoint of this enhanced MFR. This spatial coincidence suggests that the increase in B_h and decrease in F_z are most likely due to topological changes caused by reconnection rather than a change in downward momentum. Otherwise, the distribution of back-reaction responses should not show such spatial preference.

We thank the NASA SDO team for the AIA and HMI data. We also appreciate the referee for inspiring comments that improved this paper significantly. The work is supported by US NSF under grants AGS-1927578, AGS-1954737, AGS-2149748, AGS-2204384, AGS-2145253, and NASA grants 80NSSC21K1671 and 80NSSC21K0003.

ORCID iDs

Nian Liu https://orcid.org/0000-0002-6018-3799
Ju Jing https://orcid.org/0000-0002-8179-3625
Qiang Hu https://orcid.org/0000-0002-7570-2301
Satoshi Inoue https://orcid.org/0000-0001-5121-5122
Haimin Wang https://orcid.org/0000-0002-5233-565X

References

Amari, T., Luciani, J. F., Aly, J. J., & Tagger, M. 1996, ApJL, 466, L39
Antiochos, S. K., DeVore, C. R., & Klimchuk, J. A. 1999, ApJ, 510, 485
Bateman, G. 1978, MHD Instabilities (Cambridge, MA: MIT Press)
Baty, H. 2001, A&A, 367, 321
Fisher, G. H., Bercik, D. J., Welsch, B. T., & Hudson, H. S. 2012, SoPh, 277, 59
Gosain, S. 2012, ApJ, 749, 85
Hu, Q., & Dasgupta, B. 2006, GeoRL, 33, L15106
Hu, Q., & Dasgupta, B. 2008, SoPh, 247, 87
Hu, Q., Dasgupta, B., Choudhary, D. P., & Buchner, J. 2008, ApJ, 679, 848
Hu, Q., Dasgupta, B., DeRosa, M., Büchner, J., & Gary, G. 2010, JASTP, 72, 219
Hudson, H. S., Fisher, G. H., & Welsch, B. T. 2008, in ASP Conf. Ser. 383, Subsurface and Atmospheric Influences on Solar Activity, ed. R. Howe et al. (San Francisco, CA: ASP), 221
Ishiguro, N., & Kusano, K. 2017, ApJ, 843, 101
Kliem, B., & Török, T. 2006, PhRvL, 96, 255202
Kusano, K., Iju, T., Bamba, Y., & Inoue, S. 2020, Sci, 369, 587
Lemen, J. R., Title, A. M., Akin, D. J., et al. 2012, SoPh, 275, 17
Liu, C., Deng, N., Lee, J., et al. 2013, ApJL, 778, L36
Liu, C., Lee, J., Gary, D. E., & Wang, H. 2007, ApJL, 658, L127
MacNeice, P., Antiochos, S. K., Phillips, A., et al. 2004, ApJ, 614, 1028
Moore, R. L., Sterling, A. C., Hudson, H. S., & Lemen, J. R. 2001, ApJ, 552, 833
Muhamad, J., Kusano, K., Inoue, S., & Bamba, Y. 2018, ApJ, 863, 162
Muhamad, J., Kusano, K., Inoue, S., & Shiota, D. 2017, ApJ, 842, 86
Pesnell, W. D., Thompson, B. J., & Chamberlin, P. C. 2012, SoPh, 275, 3
Petrie, G. J. D. 2012, ApJ, 759, 50
Petrie, G. J. D. 2019, ApJS, 240, 11
Prasad, A., Bhattacharyya, R., & Kumar, S. 2017, ApJ, 840, 37
Priest, E. R., & Demoulin, P. 1995, JGRA, 100, 23443
Scherrer, P. H., Schou, J., Bush, R. I., et al. 2012, in The Helioseismic and Magnetic Imager (HMI) Investigation for the Solar Dynamics Observatory (SDO), ed. P. Chamberlin, W. D. Pesnell, & B. Thompson (New York: Springer), 207
Spirock, T. J., Yurchyshyn, V. B., & Wang, H. 2002, ApJ, 572, 1072
Sun, X., Hoeksema, J. T., Liu, Y., et al. 2012, ApJ, 748, 77
Titov, V. S., Hornig, G., & Démoulin, P. 2002, JGRA, 107, 1164
Tokman, M., & Bellan, P. M. 2002, ApJ, 567, 1202
Török, T., & Kliem, B. 2003, A&A, 406, 1043
Török, T., Kliem, B., & Titov, V. S. 2004, A&A, 413, L27
Wang, H. 2006, ApJ, 649, 490
Wang, H., & Liu, C. 2010, ApJL, 716, L195
Wang, H., Qiu, J., Jing, J., et al. 2004, ApJ, 605, 931
Wang, H., Spirock, T. J., Qiu, J., et al. 2002, ApJ, 576, 497
Wang, R., Liu, Y. D., Yang, Z., & Hu, H. 2014, ApJ, 791, 84
Wang, S., Liu, C., Liu, R., et al. 2012a, ApJL, 745, L17
Wang, S., Liu, C., & Wang, H. 2012b, ApJL, 757, L5
Wheatland, M. S., Sturrock, P. A., & Roumeliotis, G. 2000, ApJ, 540, 1150
Wiegelmann, T. 2004, SoPh, 219, 87
Wiegelmann, T., Inhester, B., & Sakurai, T. 2006, SoPh, 233, 215